Journal of MATERIALS RESEARCH

Article
DOI:10.1557/s43578-021-00322-2

MULTI-MATERIAL ADDITIVE MANUFACTURING

FOCUS ISSUE

Stiff and strong, lightweight bi-material sandwich plate-lattices with enhanced energy absorption

Meng-Ting Hsieh[1,b], Chan Soo Ha[2,b], Zhenpeng Xu[1], Seokpum Kim[3], H. Felix Wu[4], Vlastimil Kunc[3], Xiaoyu Zheng[1,2,5,a]

[1] Department of Civil and Environmental Engineering, University of California, Los Angeles, CA 90095, USA
[2] Department of Mechanical Engineering, Virginia Tech, Blacksburg, VA 24061, USA
[3] Manufacturing Science Division, Oak Ridge National Laboratory, Oak Ridge, TN 37831, USA
[4] Vehicle Technologies Office, U.S. Department of Energy, 1000 Independence Ave., SW, Washington, DC 20585, USA
[5] Department of Mechanical and Aerospace Engineering, University of California, Los Angeles, CA 90095, USA
[a] Address all correspondence to this author. e-mail: rayne@seas.ucla.edu
[b] These authors contributed equally to this work.

Received: 11 March 2021; accepted: 27 July 2021

Xiaoyu Zheng was an editor of this journal during the review and decision stage. For the JMR policy on review and publication of manuscripts authored by editors, please refer to http://www.mrs.org/editor-manuscripts.

Plate-based lattices are predicted to reach theoretical Hashin–Shtrikman and Suquet upper bounds on stiffness and strength. However, simultaneously attaining high energy absorption in these plate-lattices still remains elusive, which is critical for many structural applications such as shock wave absorber and protective devices. In this work, we present bi-material isotropic cubic + octet sandwich plate-lattices composed of carbon fiber-reinforced polymer (stiff) skins and elastomeric (soft) core. This bi-material configuration enhances their energy absorption capability while retaining stretching-dominated behavior. We investigate their mechanical properties through an analytical model and finite element simulations. Our results show that they achieve enhanced energy absorption approximately 2–2.8 times higher than their homogeneous counterparts while marginally compromising their stiffness and strength. When compared to previously reported materials, these materials achieve superior strength-energy absorption characteristics, making them an excellent candidate for stiff and strong, lightweight energy absorbing applications.

Introduction

Ultralight materials that are simultaneously stiff, strong, and tough (high energy absorption) are attractive. These materials (unattainable with monolithic bulk solids) can be achieved by designing the unit cell topology of a periodic, porous biphasic network (one phase is the material, ooas the other phase is the void), also known as "cellular materials" or "lattices" [1, 2], such that their effective Young's moduli, E, strength, σ (initial yield or fracture-dominated), and energy absorption, U, can be tuned over their relative density $\overline{\rho}$. While $E \sim \overline{\rho}^a$ and $\sigma \sim \overline{\rho}^b$ ($a = b = 1$ for stretching-dominated topologies; $a = 2$ and $b = 1.5$ for bending-dominated topologies) [2–4], U depends on the topology, constituent material properties, and several other factors. Owing to this linear dependence of E and σ on $\overline{\rho}$, stretching-dominated open-cell beam-based lattices, such as octet [5, 6] and cubic truss [7, 8], have dominated the lightweight material design space.

Furthermore, beam-based lattices have been manufactured by a wide variety of additive manufacturing techniques such as self-propagating polymerization waveguide (SPPW) [9, 10], powder bed fusion [11, 12], projection micro-stereolithography (PμSL) [13], and direct laser writing (DLW) [14, 15] and provided opportunities for unique combinations of constituent material and topology. However, it was shown that these open-cell beam-based lattices can only achieve fractions of the isotropic elastic limit [16] (i.e., Hashin–Shtrikman upper bound [17]). On the other hand, closed-cell plate-lattices (although more limited in suitable fabrication methods), such as

cubic + octet [18] and n-fold symmetry plate-lattices [19], have been identified to approach both isotropic upper bounds of the Young's modulus and strength at low $\overline{\rho}$ through numerical [20] and experimental [21] investigations. However, these closed-cell plate-lattices, due to their stretching-dominated deformation mode, often experience brittle fracture or exhibit a short and none-plateaued post-yield stress–strain curve [3, 22, 23] under compression at low $\overline{\rho}$, which is undesirable for energy absorbing applications. While bending-dominated lattices (for example, Kelvin foams [24–27] and hollow pyramidal lattices [28, 29]) can potentially be a good energy absorber, they show significant lower E and σ (often orders of magnitude lower), not suitable for strong, lightweight applications. As such, the simultaneous optimization of stiffness, strength, and energy absorption is not achievable by a single-material lattice.

One way to increase the energy absorption without significantly compromising the stiffness and strength of an open-cell lattice is to introduce a much softer material into its complementary void space, resulting in a bi-material interpenetrating phase composite (IPC) [30, 31]. These IPCs benefit from two topologically interconnected material phases exhibiting enhanced energy absorption by different deformation mechanisms including buckling suppression, crack resistance, or stress redistribution at the interface [32–34]. The enhanced energy absorption through IPC designs, however, have two main disadvantages: (i) the design approach is not suitable for closed-cell lattices where the bi-continuous interpenetrating layout cannot be achieved; (ii) it often comes at the cost of increasing mass [35], due to the introduction of additional topology from the second phase.

Another way to increase the energy absorption of a lattice with minimal reduction on its stiffness and strength is to apply the two material phases (stiff and soft phases) directly into the lattice topology; for instance, a beam-based lattice can have each of its beams consisting of a soft material in the center surrounded by a thin stiff material phase [36]. We hypothesize that this idea can be applied to a closed-cell plate-lattice such that each of its plates consists of a soft material ply sandwiched between two stiff material plies (analogous to a laminated composite) to achieve high energy absorption and strength. This plate configuration will potentially permit the exploitation of both stretching-dominated mechanisms and energy absorption via its two-phase composite plates. Additionally, as these material phases only occupy the original topology space, there will not be any significant increase in the lattice mass.

In this work, we present the design of bi-material isotropic cubic + octet sandwich plate-lattices, that are potentially light, stiff, and strong with enhanced energy absorption via the above-mentioned multi-material design strategy (i.e., each sandwich plate is composed of a soft material ply sandwiched between two stiff material plies). Inspired by our previous success in multi-material printing of carbon fiber reinforcement polymer (CFRP)- and soft polymer-based lattices [37], we select these two representative materials as a stiff and soft phase, respectively. First, we extend the analytical solution for linear-elastic moduli of single-material plate-lattices [18] to dynamic moduli of bi-material plate-lattices, revealing the viscoelastic effects of the embedded soft phase on their macroscopic mechanical properties. Then, we evaluate the structural performance of the plate-lattices by numerically investigating its effective modulus, peak strength, and energy absorption up to failure for different relative densities with the volume fraction of the soft phase ranging from 0 to 40%. These simulation results are cross-validated by comparing the moduli with those obtained from the analytical solutions. Lastly, we assess their strength and energy absorption performance against previously reported carbon-based architected materials.

Results and discussion

Design of the bi-material isotropic cubic + octet plate-lattice

We designed our bi-material plate-lattices by adopting the isotropic cubic + octet configuration as a baseline topology, where a cubic-plate unit cell is combined with an octet-plate unit cell (Fig. 1). The chosen configuration was motivated by (i) its stretching-dominated deformation giving rise to efficient stiffness (or strength)-to-weight ratio; (ii) its capability to achieve the theoretical Hashin–Shtrikman [17] and Suquet [38] upper bounds on stiffness and strength [18, 20, 21], respectively. We also introduced small holes at the center of the plate faces for the removal of residual (i.e., unpolymerized resin) which are needed for available additive manufacturing processes (an example is given in Appendix A). The relative density of a single-material isotropic cubic + octet plate-lattice, taking the holes into account, can be approximated as $\overline{\rho}_{\text{cubic+octet}} = (3/L - (12\pi r^2)/L^3)\cdot t_{\text{cubic}} + ((4\sqrt{3})/L - (32\pi r^2)/L^3)\cdot t_{\text{octet}}$, where L is the unit cell size, r is the radius of the holes, t_{cubic} and t_{octet} are the plate thickness of the cubic and octet unit cell, respectively [18, 20], with thickness ratio:

$$\frac{t_{\text{cubic}}}{t_{\text{octet}}} = \frac{8\sqrt{3}L^2 - 64\pi r^2}{9L^2 - 36\pi r^2} \tag{1}$$

To introduce bi-material composition to the isotropic cubic + octet plate architecture, we replaced each of its constituent plates by a two-phase sandwich plate (CFRP[1]-Soft[2]-CFRP

[1] CFRP stands for carbon fiber-reinforced polymer, a stiff and strong material (see more details in Appendix B).

[2] Soft phase is made of Flexible, a soft and weak rubber-like material (see more details in Appendix B).

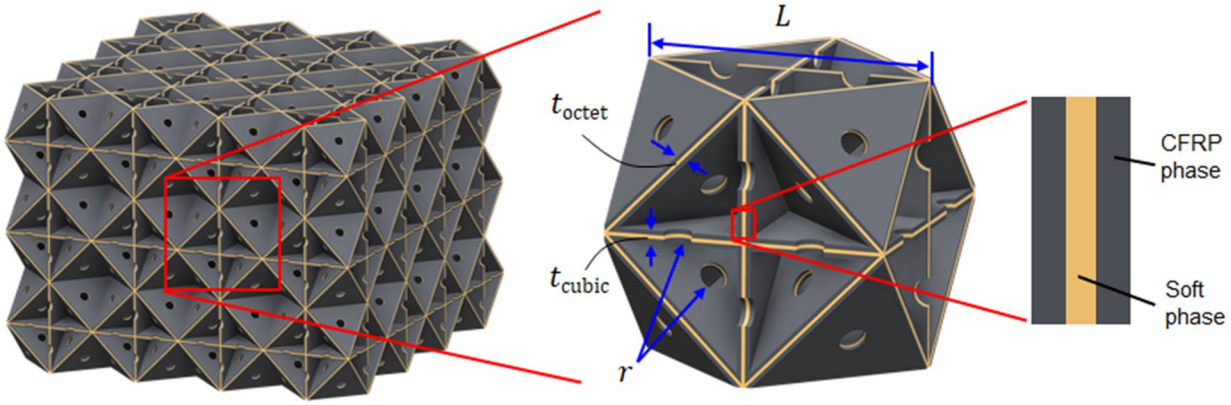

Figure 1: Illustration of bi-material isotropic cubic + octet plate-lattice with 3 × 3 × 3 unit cells. Each plate is designed as a sandwich plate (CFRP-soft-CFRP ply). To achieve isotropy, the thickness ratio is enforced as $t_{cubic}/t_{octet} = (8\sqrt{3}L^2 - 64\pi r^2)/(9L^2 - 36\pi r^2)$, where L is the unit cell side length and r is the radius of a hole at the center of the plate faces allowing the removal of unpolymerized resin after fabrication. The thicknesses of CFRP and soft phases are defined by their volume fractions such as $t_{cubic,CFRP} = V_{CFRP} \cdot t_{cubic}$, $t_{cubic,soft} = V_{soft} \cdot t_{cubic}$, $t_{octet,CFRP} = V_{CFRP} \cdot t_{octet}$, and $t_{octet,soft} = V_{soft} \cdot t_{octet}$, where $V_{CFRP} + V_{soft} = 1$.

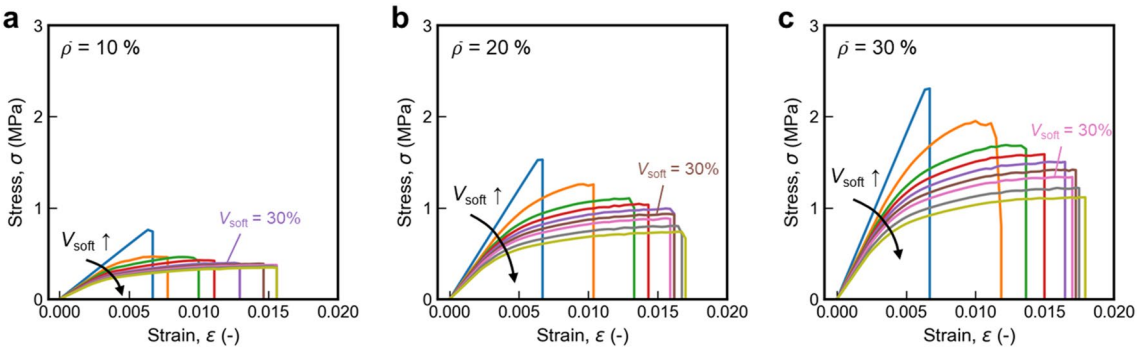

Figure 2: Simulated compressive stress–strain curves of bi-material isotropic cubic + octet plate-lattices for different relative densities, $\bar{\rho}$, with the volume fractions of the soft phase, V_{soft}, between 0 and 40%. (a) $\bar{\rho}$ = 10%, (b) $\bar{\rho}$ = 20%, (c) $\bar{\rho}$ = 30%. A stress–strain evolution from brittle response to elastoplastic-like behavior was realized through a change in V_{soft}.

ply), as shown in Fig. 1. We can then relate the total plate thickness to the thickness of each material phase through $t_{cubic,i} = V_i \cdot t_{cubic}$ and $t_{octet,i} = V_i \cdot t_{octet}$, where the subscript i denotes either CFRP or soft phase, $t_{cubic,i}$ is the ply thickness of material phase i in the cubic-plate architecture, $t_{octet,i}$ is the ply thickness of material phase i in the octet-plate architecture, and V_i is the volume fraction of the material phase i in the cubic + octet architecture. We then designed the plate-lattices with $\bar{\rho}_{cubic+octet}$ of 10, 20, and 30% and V_{soft} from 0 to 40%.

Evolution of stress–strain curves from elastic–brittle to elastoplastic response

Compressive stress–strain curves of the designed bi-material isotropic cubic + octet plate-lattices, obtained from the simulations (see the detailed material models and boundary conditions in 'Finite element simulations'), for relative densities, $\bar{\rho}$, of 10, 20, 30% with volume fractions of the soft phase, V_{soft}, between 0 and 40% are shown in Fig. 2. With an increase in V_{soft}, we observed an evolution of a stress–strain curve, changing from a linearly elastic response followed by brittle fracture to a behavior mimicking linear elastic–plastic response. This transition can be explained by examining variations in yield and failure strains and the peak strength (Figs. 9 and 2). When V_{soft} is below 30%, yield strains gradually decrease, whereas failure strains significantly increase as V_{soft} increases. By contrast, at high V_{soft} (e.g., > 30%), yield strains remain nearly constant at ~ 0.6% and failure strains progressively approach approximately 1.5% for all modeled relative densities. In addition, the magnitude of the peak strength reduces as V_{soft} increases. These interconnected variations, attributed to a change in the stiff-soft phase ratio in the constituent plate, facilitate the evolution of stress–strain curves of the plate-lattice, enabling various failure mechanisms which progressively change from brittle fracture to more ductile failure caused by plate buckling. Furthermore, when holding the stiff–soft phase ratio constant, the stiffness and strength of

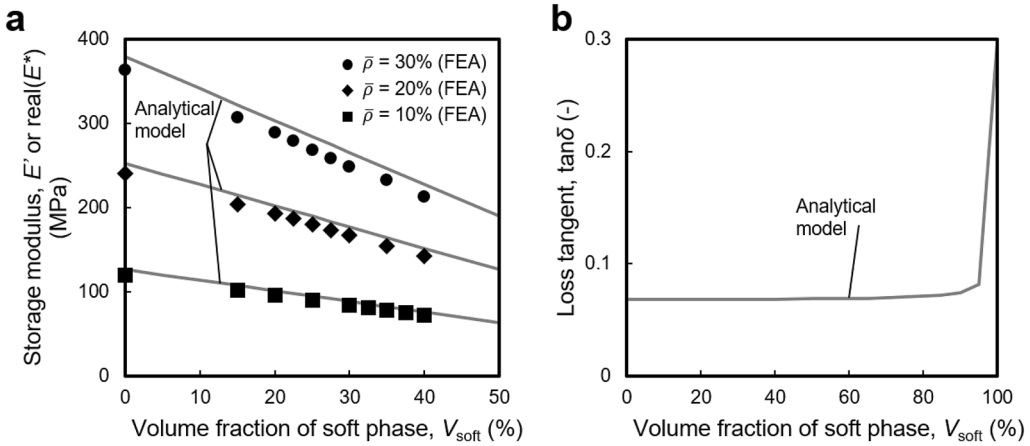

Figure 3: Effective viscoelastic properties of bi-material isotropic cubic + octet plate-lattices for $\bar{\rho}$ of 10, 20, 30% with V_{soft} between 0 and 40%. (a) Effective storage modulus, E' or real(E^*). (b) Effective loss tangent, tan δ, representing intrinsic mechanical damping. The lines in these figures are obtained from the analytical model, whereas filled markers represent results from finite element simulations.

the plate-lattices follow the power-law scaling with $\bar{\rho}$, similar to other typical cellular materials [1], and this scaling relation will be discussed later in this section.

Effective storage modulus, peak strength, and energy absorption

The effective modulus, peak strength, and absorbed energy of the bi-material isotropic cubic + octet plate-lattices were extracted from their simulated stress–strain curves. Figure 3a shows that the storage modulus, E' or real(E^*), is inversely but linearly proportional to V_{soft}. When compared with our analytical model (see the detailed formulation of the effective modulus in "Analytical derivation of the effective modulus") plotted as solid lines in Fig. 3a, E' was only slightly lower due to the holes at the center of each plate face. When fitted against $\bar{\rho}$ using least square method, near-linear scaling for the modulus was found (i.e., real(E^*) $\propto \bar{\rho}^1$) for all modeled lattices, confirming their efficient stretching-dominated behavior consistent with the previous work [21]. In addition, for the plate-lattices entirely constructed with the CFRP phase (i.e., $V_{soft} = 0\%$) for all $\bar{\rho}$ under consideration, we verified that their moduli obtained from our simulations approach the theoretical Hashin–Shtrikman upper bound of a single-material cubic + octet plate-lattice as reported previously [18]. By contrast, the magnitude of the loss modulus, E'', was found to be trivial compared to that of E' (hence low tan δ shown in Fig. 3b) when V_{soft} is below ~ 90%, justifying the constituent material models in our simulations neglecting viscoelastic effects. More specifically, the effective loss tangent, tan δ, starts from the inherent tan δ of the CFRP phase (equal to 0.068), and slowly increases with the increasing V_{soft} and then rapidly ramps up to 0.3 (equal to the inherent tan δ of the soft phase) at $V_{soft} \approx 0.9$ due to a much steeper negative slope of E' than that of with the increasing V_{soft}. We also found that the effective tan δ in a linear regime of a stress–strain curve, representing intrinsic mechanical damping, is invariant with $\bar{\rho}$ since it is the ratio of the loss modulus to storage modulus which both scale with $\bar{\rho}^1$.

Figure 4a plots the peak strength, σ_{peak}, against the volume fraction of the soft phase, V_{soft}. The strength decreases nonlinearly with an increase in V_{soft}, owing to plate buckling. With least square fitting, the strength has the scaling exponent of ~ 1 (i.e., $\sigma_{peak} \propto \bar{\rho}^1$) consistent with the reported value [21], where their strength-to-weight ratios do not substantially degrade as density decreases (i.e., efficient stretching-dominated behavior). Figure 4b reveals the absorbed energy of the bi-material plate-lattices as a function of V_{soft}, computed by integrating stress over strain in Fig. 2. This relationship does not show monotonic trends as observed in other obtained properties (E', tan δ, and σ_{peak} in Figs. 3a, b and 4a, respectively) but shows local maxima at specific V_{soft} for different relative densities. This is due to the competition between the peak strength and failure strain (Figs. 4a and 9b) attributed to plate buckling, while the latter contributes more to the overall energy absorption. For example, at $\bar{\rho} = 0.1$, failure strain rapidly increases but becomes plateau at $V_{soft} = 35\%$, whereas the peak strength only slowly decreases with an increase in V_{soft}. This combination gives rise to a concave-down curve of absorbed energy against V_{soft} (Fig. 4b), where its optimum is achieved when failure strain becomes plateau (i.e., at critical $V_{soft} = 35\%$) in the failure strain–V_{soft} plot (Fig. 9). Similarly, the critical V_{soft} results in the optimal energy absorption for other relative densities (i.e., V_{soft} of 25% and 27.5% for $\bar{\rho} = 0.2$ and 0.3, respectively). As a result, we found that the optimal absorbed energy obtained from all modeled relative densities were improved by a factor of approximately 2–2.8 compared to plate-lattices entirely made of the CFRP phase. A more accurate energy absorption estimation, which accounts the viscoelastic

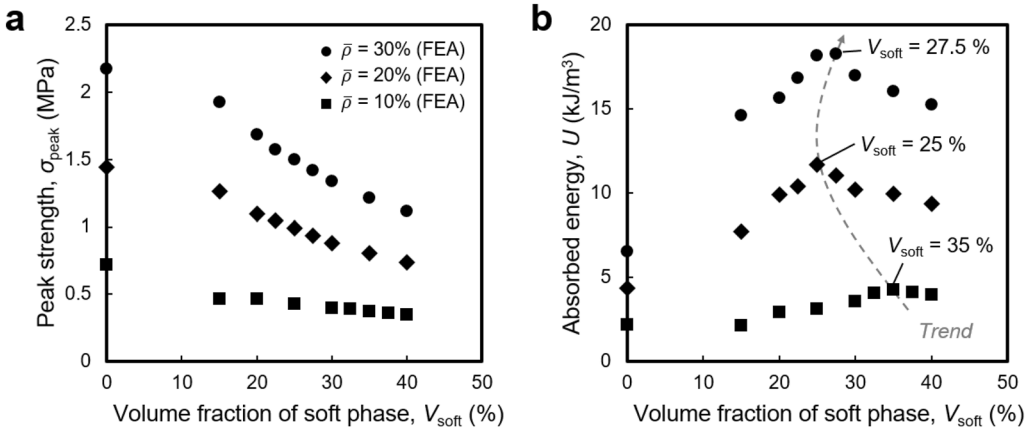

Figure 4: Simulated mechanical properties of bi-material isotropic cubic + octet plate-lattices having different V_{soft} for $\bar{\rho}$ of 10, 20, 30%. (a) Peak strength, σ_{peak}, (b) Absorbed energy, U.

contributions from the soft phase, could be accomplished if the soft phase is modeled as a viscoelastic material in the simulation, however, we believe a change would be minimal since the analytically obtained tan δ barely varies at low V_{soft} (Fig. 3b).

Assessment of strength-energy absorption performance

To assess the performance of their strength-energy absorption pair, we compared our bi-material isotropic cubic + octet plate-lattices against previously reported carbon-based architected materials (Fig. 5). We adopted normalized strength and normalized absorbed energy as a measure of strength-energy absorption characteristics (i.e., U/E_s vs. $\sigma_{peak}/\sigma_{ys}$) to highlight the roles of the cellular topology while suppressing the effects of the constituent material properties; herein, E_s and σ_{ys} for bi-material lattices represent the homogenized properties of either the constituent plate or strut made of the CFRP and soft phase and are approximated using the rule of mixture, whereas the reported values of E_s and σ_{ys} [39, 40] are used for single-material carbon-based lattices. For $\bar{\rho} \sim 10\%$, our bi-material plate-lattice, when designed with the optimal V_{soft}, exhibits the largest energy absorption (~ 0.6% over carbon microlattice [40] and ~ 312% over CF octet-truss [37]) and advantageous strength (~ 1.7 times stronger than carbon microlattice but ~ 13% weaker than CF octet-truss). Furthermore, our bi-material plate-lattices show favorable strength-energy absorption characteristics against two-phase CF octet-truss lattices [37] (e.g., advantage in U/E_s of ~ 200% and in $\sigma_{peak}/\sigma_{ys}$ of 120%) at $\bar{\rho}$ of ~ 10%. For low $\bar{\rho}$ regime (< 0.1%), we expect our bi-material plate-lattices with the optimal V_{soft}, if manufacturable, would also outperform carbon foams (bending-dominated). This is because the gain in energy absorption (dictated by both strength and failure strain) of these carbon foams are compromised by significant reduction in their strength following $\sigma \propto \bar{\rho}^2$, while the bi-material plate-lattices retain the stretching-dominated efficiency (i.e., $\sigma \propto \bar{\rho}^1$) with enhanced energy absorption due to the increased failure strain by incorporating soft material phase. CF and bi-material plate-lattices with higher $\bar{\rho}$ (10%, 20%, and 30%) are also shown in the inset in Fig. 5 to show a trend of their strength-energy absorption pairs at higher $\bar{\rho}$. This comparison implies that our bi-material plate-lattices are an excellent candidate for impact isolation and energy dissipation with simultaneously higher strength

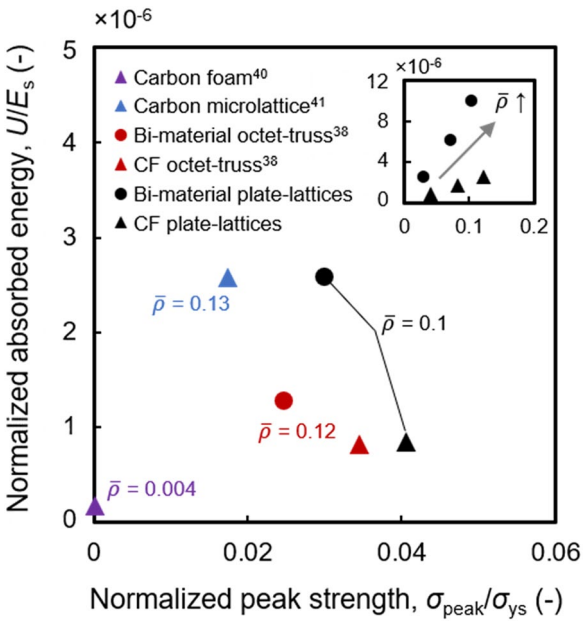

Figure 5: Performance assessment of strength-energy absorption pair of the presented bi-material isotropic plate-lattice against previously reported, carbon-based energy absorbing materials in terms of normalized absorbed energy and normalized peak strength (i.e., (U/E_s) vs. ($\sigma_{peak}/\sigma_{ys}$). CF and bi-material octet-truss adopted from Ref. [37]. Carbon foam adopted from Ref. [39]. Carbon microlattice adopted from Ref. [40].

and energy absorption. Furthermore, improvement in energy absorption of our bi-material plate-lattices is an order of magnitude larger than a reduction in strength (e.g., ~ 270% improvement in energy absorption with ~ 28% reduction in strength at $\overline{\rho}$ of 20% with V_{soft} of 25% in Fig. 4), indicating marginal degradation in their load-bearing capacity. In addition, since our study assumes that the bi-material plate-lattices are perfect (i.e., no defects, perfect bonding between the two material phases, non-porous plates, etc.), reliable multi-material manufacturing process would be desirable. Potential manufacturing techniques for realization of the presented bi-material isotropic cubic + octet plate-lattices include snap-fit method with additive manufacturing, two-photon polymerization direct laser writing with subsequent coating, and PμSL-printed shell lattices followed by soft phase injection (the last technique in Appendix A).

Conclusions

In this work, we designed bi-material isotropic plate-lattices composed of CFRP skins and a soft core arranged in a sandwich layout and derived the analytical model estimating their dynamic properties. We then investigated the stiffness, strength, and energy absorption of these plate-lattice materials modulated by changing the volume fraction of the embedded soft phase via numerical simulations, where the stiffness was verified by analytical calculations. Our results reveal that the bi-material plate-lattices, when designed with the optimal volume fraction of the soft phase, exhibit 250% (in average) increase of energy absorption with marginal reductions in modulus and strength (~ 30%) when compared to single-material CFRP plate-lattices. Furthermore, at $\overline{\rho}$ of ~ 10%, their strength and energy absorption outperform those of two-phase CF truss-based lattices (~ 120% and ~ 200%, respectively), and they are 1.7 times stronger than the carbon microlattices with comparable energy absorption. Our results reveal the roles of multi-material designs on the effective material properties of a lattice topology—a combination of the lattice topology and two-phase material configuration enables the enhanced strength-energy absorption pairs. This study will also motivate several areas of interest for future work, including acoustic isolation and impact mitigation. We envision that these bi-material enhancement on strength and energy absorption can be extended to other plate-based topologies and minimal surface-based topologies (i.e., spinodal lattices [33, 41, 42] or triply periodic minimal surfaces [43–45]) that can be realized via a wide variety of additive manufacturing methods.

Theory and simulation

Analytical derivation of the effective modulus

In the following subsections, we will extend the existing analytical solutions for the effective modulus, E, of single-material [18, 46] to bi-material isotropic plate-lattices, from which both quasi-static, E, and dynamic (viscoelasticity) moduli, E^*, can be derived. Our approach is based on the strain energy method that relates global effective properties of a lattice to the local homogenized properties of each plate via non-directional elastic strain energy density terms, hence allowing superposition even for plate- lattices constructed by dissimilar topologies.

Transverse isotropy of a bi-material sandwich plate

Each bi-material sandwich plate can be treated as a transversely isotropic plate (Fig. 6b) with five independent homogenized elastic constants E_p (in-plane Young's modulus), ν_p (Poisson's ratio for in-plane strain due to in-plane straining), ν_{pz} (Poisson's ratio for out-of-plane strain due to in-plane straining), E_z (out-of-plane Young's modulus), and G_{pz} (out-of-plane shear modulus). From the theory of elasticity, these homogenized elastic constants can be expressed in terms of the constituent materials' mechanical properties:

$$E_p = E_{s,CFRP} V_{CFRP} + E_{s,soft}(1 - V_{CFRP}) \tag{2}$$

$$\nu_p = \frac{E_{s,CFRP}\nu_{s,CFRP} V_{CFRP} - E_{s,soft}\nu_{s,soft}(1 - V_{CFRP})}{E_{s,CFRP} V_{CFRP} - E_{s,soft}(1 - V_{CFRP})} \tag{3}$$

$$\nu_{pz} = \nu_{s,CFRP} V_{CFRP} + \nu_{s,soft}(1 - V_{CFRP}) \tag{4}$$

$$E_z = \frac{E_{s,CFRP} \cdot E_{s,soft}}{E_{s,CFRP}(1 - V_{CFRP}) + E_{s,soft} V_{CFRP}} \tag{5}$$

$$G_{pz} = \frac{G_{s,CFRP} \cdot G_{s,soft}}{G_{s,CFRP}(1 - V_{CFRP}) + G_{s,soft} V_{CFRP}} \tag{6}$$

where $G_{s,CFRP}$ and $G_{s,soft}$ are the shear modulus of the CFRP and soft phases, respectively. Note that ν_{zp} (Poisson's ratio for in-plane strain due to out-of-plane straining) is equal to $\nu_{pz} \cdot E_z/E_p$ due to the symmetry of the compliance matrix.

Dynamic response of the bi-material isotropic cubic + octet sandwich plate-lattice

We then derived the effective linear-elastic modulus of the bi-material isotropic cubic + octet plate-lattice composed of the transversely isotropic plates with plane stress assumption (detailed derivations in Appendix D), given by

$$E = \frac{2(7 - 5\nu_p) E_p \overline{\rho}_{cubic+octet}}{(1 - \nu_p)(27 + 15\nu_p)} \tag{7}$$

where E_p and ν_p are given in Eqs. (2) and (3), respectively. To take viscoelastic effects into account in the analytical model, we first converted the linear-elastic moduli of the two constituent materials into the dynamic moduli (denoted by a superscript *) through the correspondence principle [47], leading to $E^*_{CFRP} = E'_{CFRP} + iE''_{CFRP}$ and $E^*_{soft} = E'_{soft} + iE''_{soft}$, where prime

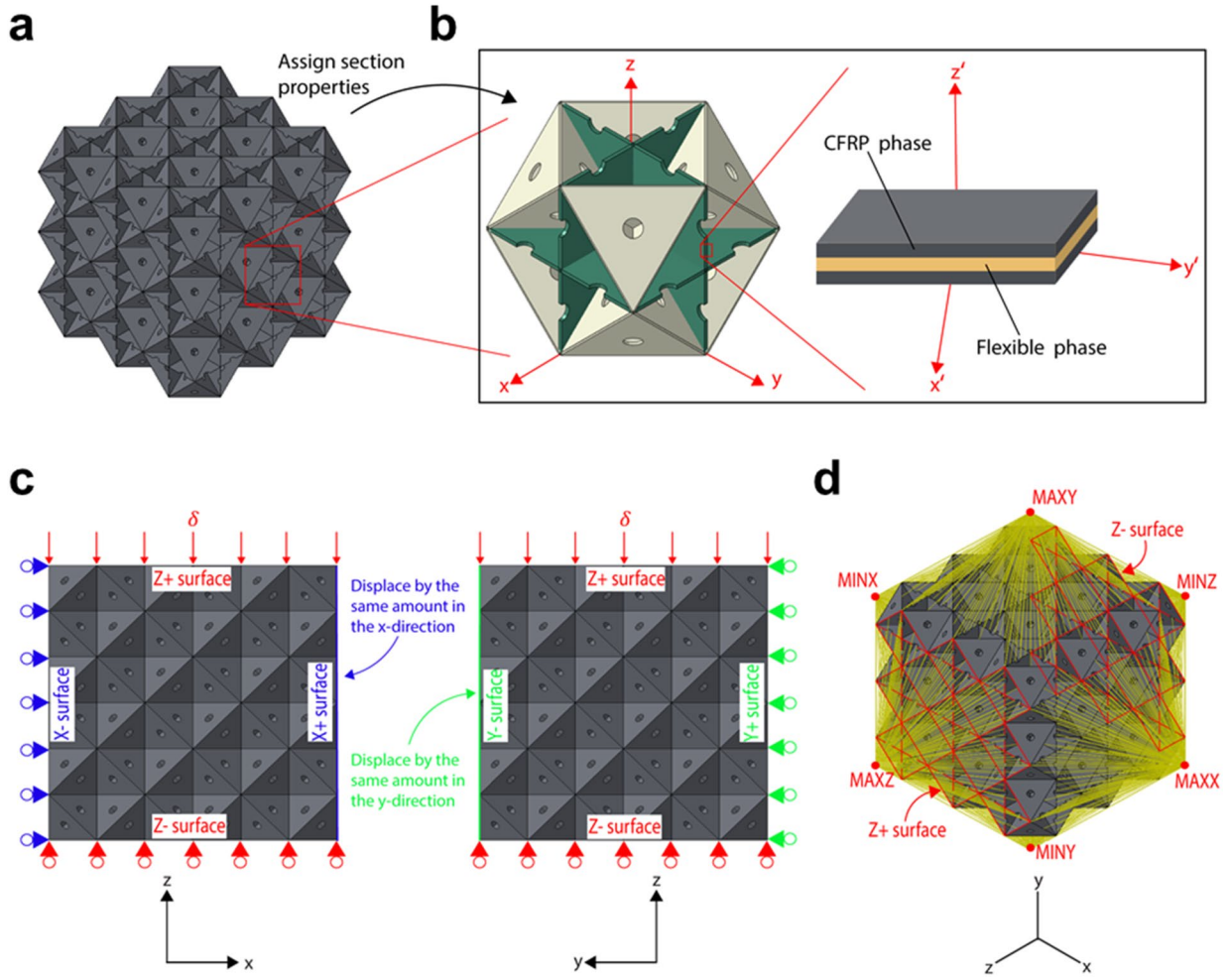

Figure 6: Illustration of the cubic + octet shell model that has (a) 3 × 3 × 3 unit cells and (b) magnified views of a single unit cell with assigned section thicknesses (dark green for the cubic-plate architecture and light yellow for the octet-plate architecture) and an individual plate with assigned section materials, under (c) quasi-periodic boundary conditions (triangles and hollow circles representing rollers) via (d) the kinematic coupling constraints (yellow light beams) between the control points (red circles) and the constrained surfaces (red highlighted surface; only one surface is highlighted for the simplicity).

(′) and double prime (″) represent the real and imaginary parts of the dynamic modulus, respectively (i.e., the storage and loss modulus, respectively). Note that "dynamic" in this context has no connection with inertial terms or resonance. By replacing the linear-elastic moduli in Eq. (2) by these dynamic terms, the dynamic modulus of the bi-material constituent plate comprising the lattice can then be written as

$$E_{\mathrm{p}}^{*} = E_{\mathrm{p}}' + iE_{\mathrm{p}}''$$
$$E_{\mathrm{p}}^{*} = V_{\mathrm{CFRP}}\left(E_{\mathrm{CFRP}}' + iE_{\mathrm{CFRP}}''\right) + (1 - V_{\mathrm{CFRP}})\left(E_{\mathrm{soft}}' + iE_{\mathrm{soft}}''\right) \quad (8)$$

Next, the effective dynamic modulus of the bi-material isotropic cubic + octet plate-lattice can be readily expressed by substituting Eq. (8) into Eq. (7) as

$$E^{*} = \frac{2(7 - 5\nu_{\mathrm{p}})}{(1 - \nu_{\mathrm{p}})(27 + 15\nu_{\mathrm{p}})} E_{p}^{*}\overline{\rho}, \quad (9)$$

where ν_{p} denotes the effective in-plane Poisson's ratio as defined in Eq. (3). Note that Eq. (9) exactly reduces to the previously derived expressions [18, 20] for linear-elastic, single-material plate-lattices when viscoelastic effects are suppressed. Lastly, the loss tangent (dimensionless), representing intrinsic mechanical damping or internal friction, can be expressed as

$$\tan\delta = \frac{\mathrm{Im}(E^{*})}{\mathrm{Re}(E^{*})} = \frac{E''}{E'} \quad (10)$$

Finite element simulations

All simulations were performed under the quasi-static condition (the kinetic energy of the whole system is assumed to be less than 5% of the internal energy in the same system) with mass scaling (scale elements that have a smaller stable time increment to the target time increment 0.005 s at the frequency of every

increment) using explicit dynamic finite element analyses in the commercial software Dassault Systemes Abaqus 2018. We used 3D shell models ($3 \times 3 \times 3$ unit cells meshed with S4R shell elements of average mesh size/L of 0.04; both determined from the convergence study in Appendix E), where the plate thickness and multi-material plies can be easily assigned in a plate-by-plate basis via the section property function, to represent the bi-material isotropic cubic + octet plate-lattice as depicted in Fig. 6. It was shown that the mechanical response between 3D shell and solid models would not differ significantly for $\overline{\rho}_{\text{cubic+octet}}$ below 40% [21]. We then investigated the mechanical response of the bi-material isotropic cubic + octet plate-lattices under compression by applying quasi-periodic boundary conditions (QPBCs) via smooth step amplitude in the time duration of 100 s to simulate response of an infinite cellular material. To obtain the effective modulus E, peak strength σ_{peak}, and energy absorption U of the plate-lattices, we first extracted the effective stress–strain (σ–ε) curve such that $\sigma = F/L^2$ and $\varepsilon = \delta/L$, where F denotes reaction force due to the applied compressive displacement δ. Then, the effective modulus E was obtained by computing a slope at an initial linear region, the peak strength σ_{peak} was taken at its maximum stress, and U was computed by calculating the area under the curve. The detailed constitutive material modeling and implementation of boundary conditions are discussed in the following subsections.

Constituent material modeling

The stiff and strong CFRP phase was modeled as a linear elastic–plastic material (Young's modulus $E_{\text{s,CFRP}} = 2.54$ GPa, Poisson's ratio $\nu_{\text{s,CFRP}} = 0.35$, and the initial yield strength $\sigma_{\text{ys,CFRP}} = 17.74$ MPa followed by isotropic hardening, $\sigma_{\text{s,CFRP}} = 17.74 + 502\varepsilon_{\text{p}}^{0.69}$ MPa, where ε_{p} is the equivalent plastic strain) that fails at a given maximum equivalent plastic strain ($\varepsilon_{\text{p,CFRP}}^{\max} = 0.00558$) while the compliant and soft phase is modeled as a linearly elastic material ($E_{\text{s,soft}} = 8.2$ MPa and $\nu_{\text{s,soft}} = 0.49$) that fails at a given maximum fracture strain ($\varepsilon_{\text{f,soft}}^{\max} = 0.37$). To simplify the material models, we suppressed the viscoelasticity effect in both CFRP and soft phases. We verified that such an assumption would not significantly change the mechanical response of the constituent materials used in this work (see Fig. 8 for the stress–strain curve comparison between simulation and experiment for both CFRP and Flexible bulk materials).

Implementation of quasi-periodic boundary conditions (QPBCs)

We implemented QPBCs (as shown in Fig. 6c) to represent an infinite plate-lattices. QPBCs allow a much simpler prescription of the displacements on very complex topologies and are more computationally efficient than the true periodic boundary conditions while achieving similar degree of accuracy [41, 48, 49]. To implement the boundary conditions in Abaqus, we used the following procedures. First, each control point was kinematically coupled to its respective constrained surface in all rotational degrees of freedom and in the translational degree of freedom along the surface normal direction (for example, MAXZ is coupled to $z+$ surface and MINZ is coupled to z-surface in the z translational degree of freedom as shown in Fig. 6d). Second, a compressive displacement δ, corresponding to an effective strain of 2% (all simulated plate-latices lost their load-carrying capacity under this strain) in the negative z-direction, was prescribed in the z translational degree of freedom of MAXZ and zero displacements are prescribed on all the other degrees of freedom of MAXZ. Third, the translation degree of freedom of MAXX along the x-direction and of MAXY along the y-direction were let free while zero displacements were prescribed on the other degrees of freedoms of control points MAXX and MAXY. Finally, zero displacements in all degrees of freedom were prescribed on the MINX, MINY, and MINZ control points.

Acknowledgments

This research was supported by the DOE Office of Energy Efficiency and Renewable Energy, Vehicle Technologies Office and used resources at the Manufacturing Demonstration Facility, a DOE-EERE User Facility at Oak Ridge National Laboratory. C. Ha, Z. Xu, M. Hsieh, and X. Zheng would also like to thank the AFOSR Air Force Office of Scientific Research (FA9550-18-1-0299) and Office of Naval Research (N00014-18-1-2553) for financial support.

Data availability

All data generated during this study are available from the corresponding author upon reasonable request.

Declarations

Conflict of interest The authors certify that they have NO affiliations with or involvement in any organization or entity with any financial interest, or non-financial interest in the subject matter or materials discussed in this manuscript.

Appendix

A: Fabrication of the bi-material isotropic cubic + octet lattices

A hollow CAD model of an isotropic cubic + octet plate-lattice with $\overline{\rho}_{\text{cubic+octet}} = 0.3$ (shown in Fig. 7) was printed in CFRP via the projection micro-stereolithography (PμSL) system developed in the previous studies [37, 50]. After printing, the

samples were cleaned in ethanol using an ultrasonic cleaner. This process was repeated several times until the trapped resin was removed entirely. The sample was then left to dry and post-cured under UV light. One of the as-fabricated samples was cut into pieces to verify that the inner hollowed channels are interconnected (Fig. 7a). To realize bi-material plate-lattices, the soft phase, comprising methacrylate monomers and oligomers and a thermal initiator (2,2′-Azobis(2-methylpropionitrile), was injected into the structure via a small hole at the top of each sample (Fig. 7a). This process was followed by thermal post-curing at 150°F for 24 h. We ground off the extra materials (over $25 \times 25 \times 25$ mm) on six faces of the samples. One sample after grinding is displayed in Fig. 7b, clearly showing the boundary of the two material phases. Note that CFRP and soft phases were strongly bonded at their interface allowing the transfer tensile/compression loads between the two phases; this was verified through experimental observations in our previous work [37].

B: Mechanical properties of the constituent materials

Development of CFRP and Flexible

Consistent with the methods used in our previous study [37], an ultraviolet (UV) curable CFRP composite was made with a UV-sensitive resin (Formlabs Rigid, Formlabs Inc) reinforced with 5 vol% short carbon fibers (PC100, E&L Enterprises, Inc). A high-energy ball mill was used to mix the monomer and carbon fiber thoroughly. The resulting CFRP composites are stiffer than the monomer, benefiting from the high stiffness of the carbon fibers and the interfacial friction [51–53] between fibers and monomer. On the other hand, the soft material was composed of methacrylate monomers and oligomers (Formlabs Flexible, Formlabs Inc) and a thermal initiator 2,2′-Azobis(2-methylpropionitrile) (Sigma-Aldrich).

Mechanical testing

To quantify the mechanical properties of CFRP and soft materials, we built ASTM standard (D3039) bulk samples to test along the same built direction via projection micro-stereolithography (PμSL). Two mechanical testing methods were performed: uniaxial tension and dynamic mechanical analysis (DMA). The uniaxial tension tests were performed using an Instron 5944 equipped with Bluehill data acquisition software and a 2000 N load cell to evaluate the stress–strain curve of the base material. A strain rate of 10^{-3}/s (quasi-static strain rate) was conducted on each sample until fracture. The dynamic mechanical properties (storage and loss modulus) of the constituent materials were measured via a DMA apparatus (TA Instruments DMA 850) at 0.1 Hz (equivalent frequency for quasi-static condition [29]). The measured material properties are listed in Table 1; the measured stress–strain curves under uniaxial tension are compared with those obtained via constituent material modeling (see 'Constituent material modeling') in Fig. 8.

C: Yield and failure strains of the bi-material isotropic cubic + octet plate-lattices

Figure 9 shows yield and failure strains of the bi-material isotropic cubic + octet plate-lattices that were obtained from simulated stress–strain curves in Fig. 2.

D: Quasi-static response of the isotropic bi-material cubic + octet sandwich plate-lattice

Consider a cubic + octet unit cell oriented in a global Cartesian coordinate system as shown in Fig. 6b. We apply two different strain fields separately as follows:

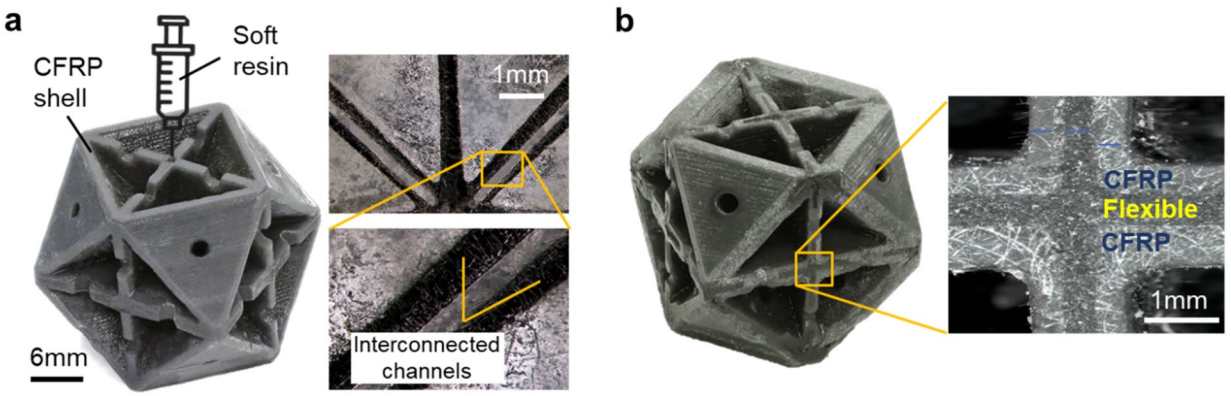

Figure 7: Fabrication of bi-material isotropic cubic + octet plate-lattices. (a) Schematic of the injection thermal curing method. Soft resin is injected into the 3D-printed octet-cubic shell made by CFRP then cured via heating. (b) Photograph showing the printed sample after injection and sanding.

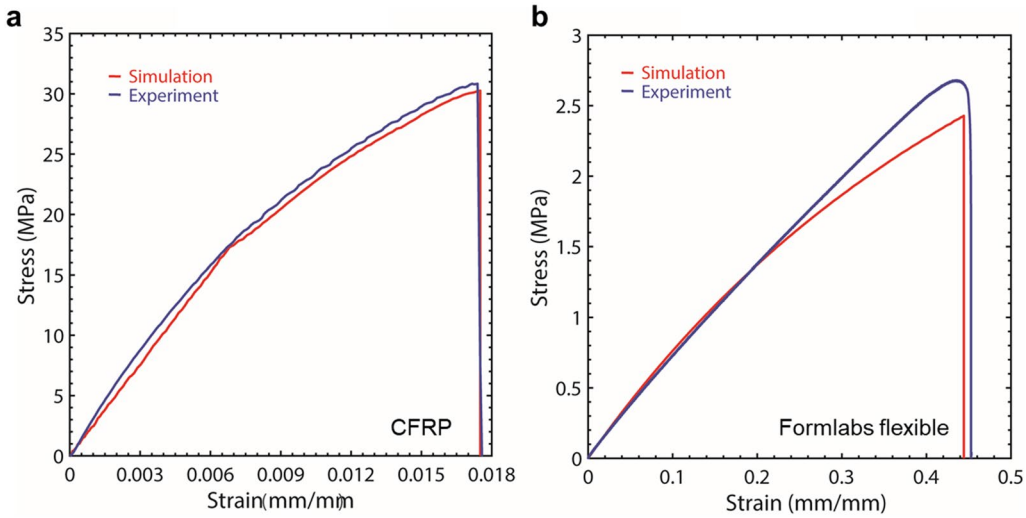

Figure 8: The comparison of the tensile stress–strain curves between the simulation and experiment for CFRP and Formlabs flexible constituent materials under uniaxial tension.

TABLE 1: Bulk material properties.

Material	Storage modulus[a], E' (MPa)	Loss modulus[a], E'' (MPa)	Loss tangent[a], tan δ (–)	Yield strength[b], σ_y (MPa)	Poisson's ratio[b], ν (–)
CFRP	2534.1	172.4	0.068	17.74	0.35
Formlabs flexible	8.2	2.4	0.299	–	0.49

[a]Measured by DMA apparatus at 0.1 Hz.

[b]Measured from uniaxial tensile test.

Uniaxial strain ($\varepsilon_{xx} = \varepsilon_{yy} = \varepsilon_{xy} = \varepsilon_{xz} = \varepsilon_{yz} = 0$ and $\varepsilon_{zz} = \varepsilon$)

First, we transform the uniaxial strain tensor from global xyz coordinate to each plate's local $x'y'z'$ coordinate. Second, we enforce the plane-stress condition and obtain the principal stress (σ_I, σ_{II}, and σ_{III}) and principal strain (ε_I, ε_{II}, and ε_{III}) components. Strain energy density of each plate then can be calculated via $U_{el} = \frac{1}{2}(\sigma_I\varepsilon_I + \sigma_{II}\varepsilon_{II} + \sigma_{III}\varepsilon_{III})$. This leads to the effective strain energy density of the unit cell under uniaxial strain as

$$U_{el,cubic+octet,uni} = \frac{E_p(2\overline{\rho}_{octet} + 3\overline{\rho}_{cubic})\varepsilon^2}{9\left(1-\nu_p^2\right)} \quad (11)$$

Hydrostatic strain ($\varepsilon_{xy} = \varepsilon_{xz} = \varepsilon_{yz} = 0$ and $\varepsilon_{xx} = \varepsilon_{yy} = \varepsilon_{zz} = \varepsilon$)

Similarly, we obtain the effective strain energy density of the unit cell under hydrostatic strain as

$$U_{el,cubic+octet,hydro} = \frac{E_p(\overline{\rho}_{octet} + \overline{\rho}_{cubic})\varepsilon^2}{1-\nu_p} \quad (12)$$

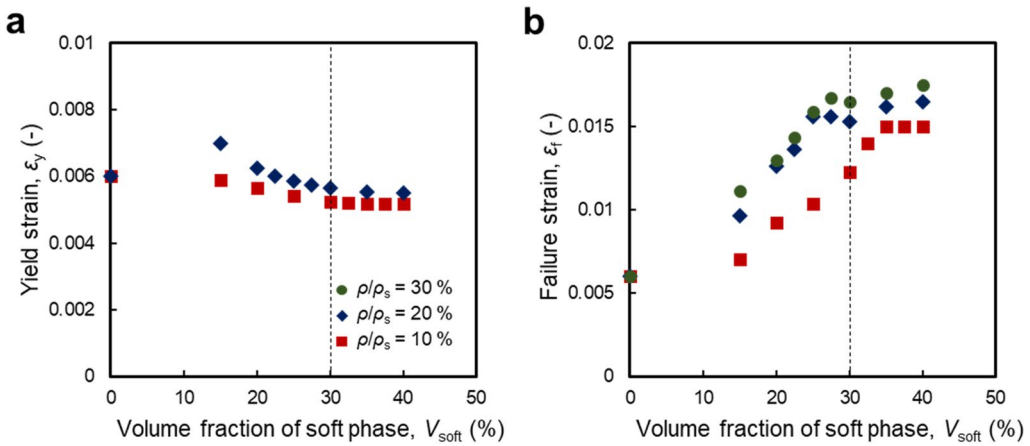

Figure 9: Yield and failure strains measured from simulated stress–strain curves of bi-material isotropic cubic + octet plate-lattices.

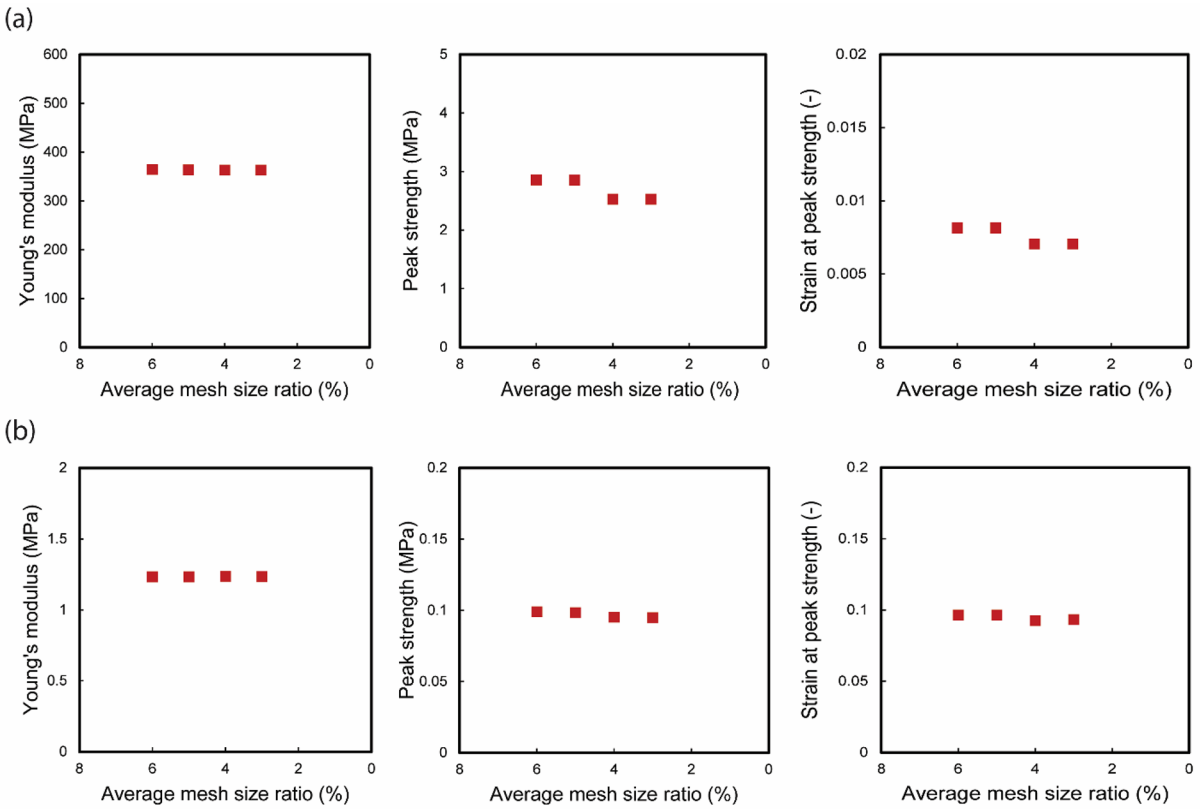

Figure 10: The Young's modulus, peak strength, and strain at peak strength of the isotropic cubic + octet plate-lattice with $\overline{\rho}_{\text{cubic+octet}} = 0.3$, made of (a) 100% volume fraction of CFRP, $V_{\text{CFRP}} = 1$ or (b) 100% volume fraction of the soft phase ($V_{\text{soft}} = 1$) is plotted against the decreasing average mesh ratio for the mesh convergence study.

Once we obtain the effective strain energy density of the unit cell, we enforce the isotropy with $\overline{\rho}_{\text{cubic}} = \frac{2}{3}\overline{\rho}_{\text{octet}}$ [19, 21]. Equations (11)–(12) are then reduced to

$$U_{\text{el,cubic+octet,uni}} = \frac{4E_{\text{p}}\overline{\rho}_{\text{cubic+octet}}\varepsilon^2}{15\left(1-\nu_{\text{p}}^2\right)} \tag{13}$$

$$U_{\text{el,cubic+octet,hydro}} = \frac{E_{\text{p}}\overline{\rho}_{\text{cubic+octet}}\varepsilon^2}{\left(1-\nu_{\text{p}}\right)} \tag{14}$$

Since the unit cell is isotropic, we can write the effective constitutive relation as follows:

$$\begin{pmatrix}\sigma_{xx}\\ \sigma_{yy}\\ \sigma_{zz}\\ \tau_{yz}\\ \tau_{xz}\\ \tau_{xy}\end{pmatrix} = \begin{bmatrix} C_{11} & C_{12} & C_{12} & & & \\ & C_{11} & C_{12} & & \text{Symm} & \\ & & C_{11} & & & \\ & & & \frac{C_{11}-C_{12}}{2} & & \\ & \text{Symm} & & & \frac{C_{11}-C_{12}}{2} & \\ & & & & & \frac{C_{11}-C_{12}}{2} \end{bmatrix} \begin{pmatrix}\varepsilon_{xx}\\ \varepsilon_{yy}\\ \varepsilon_{zz}\\ 2\varepsilon_{yz}\\ 2\varepsilon_{xz}\\ 2\varepsilon_{xy}\end{pmatrix}, \tag{15}$$

where $C_{11} = 2U_{\text{el,cubic+octet,uni}}/\varepsilon^2$ and $C_{11} + 2C_{12} = 2U_{\text{el,cubic+octet,hydro}}/\left(3\varepsilon^2\right)$. Using Eqs. (13) and (14), we can obtain elastic constants C_{11} and C_{12} as

$$C_{11} = \frac{8E_{\text{p}}\overline{\rho}_{\text{cubic+octet}}}{15\left(1-\nu_{\text{p}}^2\right)} \tag{16}$$

$$C_{12} = \frac{E_{\text{p}}\overline{\rho}_{\text{cubic+octet}}\left(1+5\nu_{\text{p}}\right)}{15\left(1-\nu_{\text{p}}^2\right)} \tag{17}$$

Finally, using $E = (C_{11} - C_{12}) \cdot (C_{11} + 2C_{12})/(C_{11} + C_{12})$, we can obtain the linearly elastic effective modulus as

$$E = \frac{2\left(7-5\nu_{\text{p}}\right)E_{\text{p}}\overline{\rho}_{\text{cubic+octet}}}{\left(1-\nu_{\text{p}}\right)\left(27+15\nu_{\text{p}}\right)}, \tag{18}$$

where E_{p} and ν_{p} were defined in Eqs. (2) and (3), respectively.

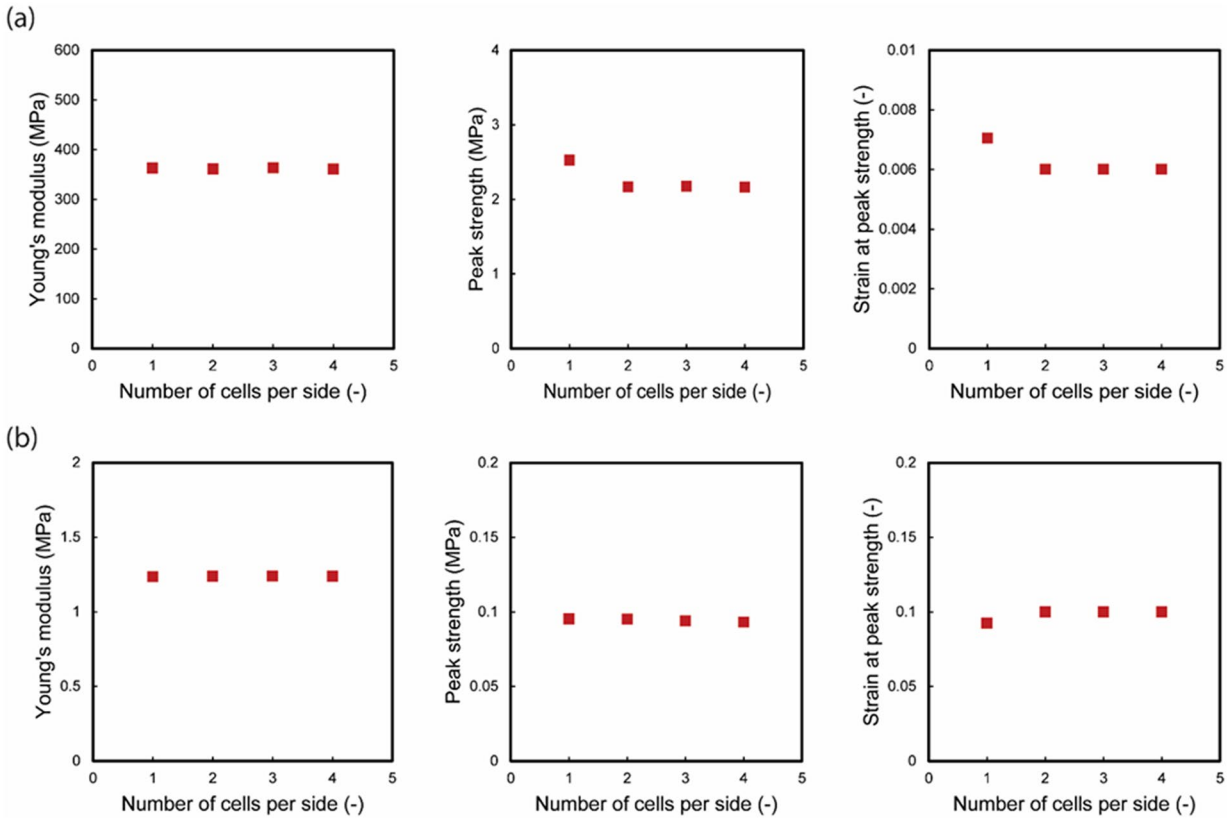

Figure 11: The Young's modulus, peak strength, and strain at peak strength of the isotropic cubic + octet plate-lattice with $\overline{\rho}_{\text{cubic+octet}} = 0.3$, made of (a) 100% volume fraction of CFRP, $V_{\text{CFRP}} = 1$ or (b) 100% volume fraction of the soft phase ($V_{\text{soft}} = 1$) is plotted against the increasing number of unit cells per side for the unit cell convergence study.

E: Convergence study

Since both buckling and fractures can occur in the simulations (two situations that can break the material symmetry required for periodic boundary conditions[3]), we first performed both the mesh and unit cell convergence studies and determined that a $3 \times 3 \times 3$ lattice configuration and an average mesh size ratio $\tilde{e}_{\text{avg}}$ (the ratio of the average element size to the unit cell size) of 0.04 are close to the converged values (see Figs. 10 and 11). The determined number of unit cells and mesh size ratio were then used in all simulations of the isotropic cubic + octet lattices with $\overline{\rho}_{\text{cubic+octet}} = 0.1$, 0.2, and 0.3 and several V_{soft} from 0 to 40% under compression.

Quasi-periodic boundary conditions (QPBCs) discussed in "Finite element simulations" were used in Abaqus to perform both the mesh and the unit cell convergence study on the isotropic cubic + octet lattice shell models with $\overline{\rho}_{\text{cubic+octet}} = 0.3$. For each convergence study, two constituent materials (100% volume fraction of CFRP, $V_{\text{CFRP}} = 1$ or 100% volume fraction of soft phase, $V_{\text{soft}} = 1$) are considered, hence representing two extreme ends of material behaviors. In the case of CFRP, a displacement δ, corresponding to 2% effective strain, is applied in the QPBCs; in the case of soft phase, a δ, corresponding to 10% effective strain is applied instead. The details are discussed below:

Mesh convergence study

Only a single unit cell was used. The average mesh size ratio $\tilde{e}_{\text{avg}}$ was then refined from 0.06 to 0.03 to study the convergence of Young's modulus, peak strength, and strain at the peak strength. $\tilde{e}_{\text{avg}} = 0.04$ was deemed appropriate for all cases (Fig. 10a and b) and then used in the unit cell convergence study.

Unit cell convergence study

The chosen average mesh size ratio $\tilde{e}_{\text{avg}} = 0.04$ was used to mesh the models and the number of unit cell was increased cubically from $1 \times 1 \times 1$ to $4 \times 4 \times 4$ to study the convergence of Young's modulus, peak strength, and strain at the peak strength. The optimal number of unit cells is determined to be $3 \times 3 \times 3$ from Fig. 11.

[3] For example, large number of unit cells are often required to investigate the crack propagations and fractures in cellular materials [54, 55].

References

1. L.J. Gibson, M.F. Ashby, *Cellular Solids: Structure and Properties* (Cambridge University Press, Cambridge, 1997)
2. N.A. Fleck, V.S. Deshpande, M.F. Ashby, Micro-architectured materials: past, present and future. Proc. R. Soc. A Math. Phys. Eng. Sci. **466**(2121), 2495 (2010)
3. V.S. Deshpande, M.F. Ashby, N.A. Fleck, Foam topology: bending versus stretching dominated architectures. Acta Mater. **49**(6), 1035 (2001)
4. M. Ashby, The properties of foams and lattices. Philos. Trans. R. Soc. A Math. Phys. Eng. Sci. **364**(1838), 15 (2006)
5. V.S. Deshpande, N.A. Fleck, M.F. Ashby, Effective properties of the octet-truss lattice material. J. Mech. Phys. Solids **49**(8), 1747 (2001)
6. L. Dong, V. Deshpande, H. Wadley, Mechanical response of Ti-6Al-4V octet-truss lattice structures. Int. J. Solids Struct. **60**, 107 (2015)
7. P.F. Egan, V.C. Gonella, M. Engensperger, S.J. Ferguson, K. Shea, Computationally designed lattices with tuned properties for tissue engineering using 3D printing. PLoS ONE **12**(8), 1 (2017)
8. J. Favre, P. Lohmuller, B. Piotrowski, S. Kenzari, P. Laheurte, F. Meraghni, A continuous crystallographic approach to generate cubic lattices and its effect on relative stiffness of architectured materials. Addit. Manuf. **21**(February), 359 (2018)
9. T.A. Schaedler, A.J. Jacobsen, A. Torrents, A.E. Sorensen, J. Lian, J.R. Greer, L. Valdevit, W.B. Carter, Ultralight metallic microlattices. Science **334**(6058), 962 (2011)
10. A.J. Jacobsen, W. Barvosa-Carter, S. Nutt, Micro-scale truss structures formed from self-propagating photopolymer waveguides. Adv. Mater. **19**(22), 3892 (2007)
11. A. El Elmi, D. Melancon, M. Asgari, L. Liu, D. Pasini, Experimental and numerical investigation of selective laser melting–induced defects in Ti–6Al–4V octet truss lattice material: the role of material microstructure and morphological variations. J. Mater. Res. **35**(15), 1900 (2020)
12. A. Ferrigno, F. Di Caprio, R. Borrelli, F. Auricchio, A. Vigliotti, The mechanical strength of Ti-6Al-4V columns with regular octet microstructure manufactured by electron beam melting. Materialia **5**, 100232 (2019)
13. X. Zheng, W. Smith, J. Jackson, B. Moran, H. Cui, D. Chen, J. Ye, N. Fang, N. Rodriguez, T. Weisgraber, C.M. Spadaccini, Multiscale metallic metamaterials. Nat. Mater. **15**(10), 1100 (2016)
14. L.R. Meza, G.P. Phlipot, C.M. Portela, A. Maggi, L.C. Montemayor, A. Comella, D.M. Kochmann, J.R. Greer, Reexamining the mechanical property space of three-dimensional lattice architectures. Acta Mater. **140**, 424 (2017)
15. L.R. Meza, S. Das, J.R. Greer, Strong, lightweight, and recoverable three-dimensional. Science **345**(6202), 1322 (2014)
16. R.M. Christensen, Mechanics of cellular and other low-density materials. Int. J. Solids Struct. **37**(1–2), 93 (2000)
17. Z. Hashin, S. Shtrikman, A variational approach to the theory of the elastic behaviour of multiphase materials. J. Mech. Phys. Solids **11**(2), 127 (1963)
18. J.B. Berger, H.N.G. Wadley, R.M. Mcmeeking, Mechanical metamaterials at the theoretical limit of isotropic elastic stiffness. Nature **1**, 533–537 (2017)
19. Y. Wang, O. Sigmund, Quasiperiodic mechanical metamaterials with extreme isotropic stiffness. Extrem. Mech. Lett. **34**, 100596 (2020)
20. T. Tancogne-Dejean, M. Diamantopoulou, M.B. Gorji, C. Bonatti, D. Mohr, 3D plate-lattices: an emerging class of low-density metamaterial exhibiting optimal isotropic stiffness. Adv. Mater. **30**(45), 1803334 (2018)
21. C. Crook, J. Bauer, A. Guell Izard, C. Santos de Oliveira, J. Martins de Souza e Silva, J.B. Berger, L. Valdevit, Plate-nanolattices at the theoretical limit of stiffness and strength. Nat. Commun. **11**(1), 1 (2020)
22. A. Schroer, J.M. Wheeler, R. Schwaiger, Deformation behavior and energy absorption capability of polymer and ceramic-polymer composite microlattices under cyclic loading. J. Mater. Res. **33**(3), 274 (2018)
23. M.A. Kader, P.J. Hazell, A.D. Brown, M. Tahtali, S. Ahmed, J.P. Escobedo, M. Saadatfar, Novel design of closed-cell foam structures for property enhancement. Addit. Manuf. **31**, 100976 (2020)
24. G. Gao, M. Qi, Y. Li, Random equilateral Kelvin open-cell foam microstructures: cross-section shapes, compressive behavior, and isotropic characteristics. J. Cell. Plast. **54**(1), 53 (2018)
25. J. Brennan-Craddock, D. Brackett, R. Wildman, R. Hague, The design of impact absorbing structures for additive manufacture. J. Phys. Conf. Ser. **382**, 012042 (2012)
26. W.-Y. Jang, S. Kyriakides, A.M. Kraynik, On the compressive strength of open-cell metal foams with Kelvin and random cell structures. Int. J. Solids Struct. **47**(21), 2872 (2010)
27. L. Gong, S. Kyriakides, W.-Y. Jang, Compressive response of open-cell foams. Part I: Morphology and elastic properties. Int. J. Solids Struct. **42**(5–6), 1355 (2005)
28. A. Torrents, T.A. Schaedler, A.J. Jacobsen, W.B. Carter, L. Valdevit, Characterization of nickel-based microlattice materials with structural hierarchy from the nanometer to the millimeter scale. Acta Mater. **60**(8), 3511 (2012)
29. L. Salari-Sharif, T.A. Schaedler, L. Valdevit, Energy dissipation mechanisms in hollow metallic microlattices. J. Mater. Res. **29**(16), 1755 (2014)
30. D.R. Clarke, Interpenetrating phase composites. J. Am. Ceram. Soc. **75**(4), 739 (1992)
31. L.D. Wegner, L.J. Gibson, The mechanical behaviour of interpenetrating phase composites—I: modelling. Int. J. Mech. Sci. **42**(5), 925 (2000)

32. J. Lee, L. Wang, M.C. Boyce, E.L. Thomas, Periodic bicontinuous composites for high specific energy absorption. Nano Letters **12**, 4392–4396 (2012)
33. Y. Zhang, M.-T. Hsieh, L. Valdevit, Mechanical performance of 3D printed interpenetrating phase composites with spinodal topologies. Compos. Struct. (2021). https://doi.org/10.1016/j.compstruct.2021.113693
34. O. Al-Ketan, M. Adel Assad, R.K. Abu Al-Rub, Mechanical properties of periodic interpenetrating phase composites with novel architected microstructures. Compos. Struct. **176**, 9 (2017)
35. Y. Liu, L. Wang, Enhanced stiffness, strength and energy absorption for co-continuous composites with liquid filler. Compos. Struct. **128**, 274 (2015)
36. L. Salari-Sharif, T.A. Schaedler, L. Valdevit, Hybrid hollow microlattices with unique combination of stiffness and damping. J. Eng. Mater. Technol. (2018). https://doi.org/10.1115/1.4038672
37. Z. Xu, C.S. Ha, R. Kadam, J. Lindahl, S. Kim, H.F. Wu, V. Kunc, X. Zheng, Additive manufacturing of two-phase lightweight, stiff and high damping carbon fiber reinforced polymer microlattices. Addit. Manuf. **32**, 101106 (2020)
38. P.M. Suquet, Overall potentials and extremal surfaces of power law or ideally plastic composites. J. Mech. Phys. Solids **41**(6), 981 (1993)
39. S. Chen, G. He, H. Hu, S. Jin, Y. Zhou, Y. He, S. He, F. Zhao, H. Hou, Elastic carbon foam via direct carbonization of polymer foam for flexible electrodes and organic chemical absorption. Energy Environ. Sci. **6**(8), 2435 (2013)
40. A.J. Jacobsen, S. Mahoney, W.B. Carter, S. Nutt, Vitreous carbon micro-lattice structures. Carbon N. Y. **49**(3), 1025 (2011)
41. M.-T. Hsieh, B. Endo, Y. Zhang, J. Bauer, L. Valdevit, The mechanical response of cellular materials with spinodal topologies. J. Mech. Phys. Solids **125**, 401 (2019)
42. C.M. Portela, A. Vidyasagar, S. Krödel, T. Weissenbach, D.W. Yee, J.R. Greer, D.M. Kochmann, Extreme mechanical resilience of self-assembled nanolabyrinthine materials. Proc. Natl. Acad. Sci. U. S. A. **117**(11), 5686 (2020)
43. M.-T. Hsieh, L. Valdevit, Minisurf—a minimal surface generator for finite element modeling and additive manufacturing. Softw. Impacts **6**, 100026 (2020)
44. M.-T. Hsieh, L. Valdevit, Update (2.0) to MiniSurf—a minimal surface generator for finite element modeling and additive manufacturing. Softw. Impacts **6**, 100035 (2020)
45. D.W. Abueidda, M. Elhebeary, C.S. Shiang, R.K. Abu Al-Rub, I.M. Jasiuk, Compression and buckling of microarchitectured Neovius-lattice. Extrem. Mech. Lett. **37**, 1006 (2020)
46. J.L. Grenestedt, Effective elastic behavior of some models for perfect cellular solids. Int. J. Solids Struct. **36**(10), 1471 (1999)
47. R. Lakes, *Viscoelastic Materials* (Cambridge University Press, Cambridge, 2009)
48. L. Valdevit, S.W. Godfrey, T.A. Schaedler, A.J. Jacobsen, W.B. Carter, Compressive strength of hollow microlattices: experimental characterization, modeling, and optimal design. J. Mater. Res. **28**(17), 2461 (2013)
49. M.-T. Hsieh: Mechanics of Minimal Surface-Based Architected Materials, UC Irvine, 2020.
50. R. Hensleigh, H. Cui, Z. Xu, J. Massman, D. Yao, J. Berrigan, X. Zheng, Charge-programmed three-dimensional printing for multi-material electronic devices. Nat. Electron. **3**(4), 216 (2020)
51. M. Invernizzi, G. Natale, M. Levi, S. Turri, G. Griffini, UV-assisted 3D printing of glass and carbon fiber-reinforced dual-cure polymer composites. Materials (Basel) **9**(7), 583 (2016)
52. H.L. Tekinalp, V. Kunc, G.M. Velez-Garcia, C.E. Duty, L.J. Love, A.K. Naskar, C.A. Blue, S. Ozcan, Highly oriented carbon fiber–polymer composites via additive manufacturing. Compos. Sci. Technol. **105**, 144 (2014)
53. X. Tian, T. Liu, C. Yang, Q. Wang, D. Li, Interface and performance of 3D printed continuous carbon fiber reinforced PLA composites. Compos. Part A Appl. Sci. Manuf. **88**, 198 (2016)
54. M.R. O'Masta, L. Dong, L. St-Pierre, H.N.G. Wadley, V.S. Deshpande, The fracture toughness of octet-truss lattices. J. Mech. Phys. Solids **98**, 271 (2017)
55. M.-T. Hsieh, V.S. Deshpande, L. Valdevit, A versatile numerical approach for calculating the fracture toughness and R-curves of cellular materials. J. Mech. Phys. Solids **138**, 103925 (2020)